frontiers in Physics

ORIGINAL RESEARCH
published: 20 July 2021
doi: 10.3389/fphy.2021.705438

Recent Advances and Challenges in the Development of Radiofrequency HTS Coil for MRI

Aimé Labbé[1], Gilles Authelet[2], Bertrand Baudouy[2], Cornelis J. van der Beek[3], Javier Briatico[4], Luc Darrasse[1] and Marie Poirier-Quinot[1]**

[1]*Université Paris-Saclay, CEA, CNRS, Inserm, Laboratoire d'Imagerie Biomédicale Multimodale Paris Saclay, Orsay, France,* [2]*Université Paris-Saclay, CEA, Département des Accélérateurs, de Cryogénie et de Magnétisme, Gif-sur-Yvette, France,* [3]*Université Paris-Saclay, CNRS, Centre de Nanosciences et de Nanotechnologies, Palaiseau, France,* [4]*Unité mixte de physique, CNRS, Thales, Université Paris-Saclay, Palaiseau, France*

OPEN ACCESS

Edited by:
Simone Angela S. Winkler, Cornell University, United States

Reviewed by:
Michael D. Noseworthy, McMaster University, Canada
Sigrun Roat, Medical University of Vienna, Austria
Elizaveta Motovilova, Weill Cornell Medicine, United States

***Correspondence:**
Aimé Labbé
aime.labbe@universite-paris-saclay.fr
Marie Poirier-Quinot
marie.poirier-quinot@universite-paris-saclay.fr

Specialty section:
This article was submitted to Medical Physics and Imaging, a section of the journal Frontiers in Physics

Received: *05 May 2021*
Accepted: *24 June 2021*
Published: *20 July 2021*

Citation:
Labbé A, Authelet G, Baudouy B, van der Beek CJ, Briatico J, Darrasse L and Poirier-Quinot M (2021) Recent Advances and Challenges in the Development of Radiofrequency HTS Coil for MRI. Front. Phys. 9:705438. doi: 10.3389/fphy.2021.705438

Radiofrequency (RF) coils fashioned from high-temperature superconductor (HTS) have the potential to increase the sensitivity of the magnetic resonance imaging (MRI) experiment by more than a dozen times compared to conventional copper coils. Progress, however, has been slow due to a series of technological hurdles. In this article, we present the developments that recently led to new perspectives for HTS coil in MRI, and challenges that still need to be solved. First, we recall the motivations for the implementations of HTS coils in MRI by presenting the limits of cooled copper coil technology, such as the anomalous skin effect limiting the decrease of the electric resistance of normal conductors at low temperature. Then, we address the progress made in the development of MRI compatible cryostats. New commercially available low-noise pulsed-tube cryocoolers and new materials removed the need for liquid nitrogen-based systems, allowing the design of cryogen-free and more user-friendly cryostats. Another recent advance was the understanding of how to mitigate the imaging artifacts induced by HTS diamagnetism through field cooling or temperature control of the HTS coil. Furthermore, artifacts can also originate from the RF field coupling between the transmission coil and the HTS reception coil. Here, we present the results of an experiment implementing a decoupling strategy exploiting nonlinearities in the electric response of HTS materials. Finally, we discuss the potential applications of HTS coils in bio-imaging and its prospects for further improvements. These include making the technology more user-friendly, implementing the HTS coils as coil arrays, and proposing solutions for the ongoing issue of decoupling. HTS coil still faces several challenges ahead, but the significant increase in sensitivity it offers lends it the prospect of being ultimately disruptive.

Keywords: high temperature superconductor, magnetic resonance imaging, MRI compatible cryostat, nonlinear properties of superconductors, HTS coil, cryogenics, imaging artefact

INTRODUCTION

The discovery of high-temperature superconductivity (HTS) by [1], paved the way for the application of superconductor-based technologies at temperatures above that of boiling nitrogen. Simultaneously, powerful, low vibration, reliable cryocoolers have been developed for applications at temperatures close to 90 K, the critical temperature of high-temperature superconducting $YBa_2Cu_3O_7$ (YBCO) which is the technologically most useful HTS material. In microwave technology, HTS has allowed the design of detectors and filters of unmatched sensitivity/selectivity and noise figures, suitable for satellite telecommunications [2]. A down-to-earth application of HTS materials is Magnetic Resonance Imaging (MRI). Here, the use of HTS materials can be envisioned both as magnet coils and as probes for the detection of the radiofrequency (RF) MR signal. The vanishing electric resistance of the superconducting MRI coil brings electric noise levels within reach that are unachievable with more traditional copper coils, even if the latter are cooled to much lower temperatures than the HTS coil; typically, the signal-to-noise ratio (SNR) can be increased more than a dozen times [3]. In spite of the promise held, the development of HTS radiofrequency MRI coils, starting from early prototypes in the 90s [4], has been slow. Interest in this technology faded in the 2000s due to technological deadlocks that seemed insurmountable at the time. These included drawbacks such as having to employ wet cryostats (e.g. using liquid nitrogen or LN_2), as well as the necessary decoupling of the RF detection coil (fashioned from a HTS material) from the (copper) RF transmission coil. Both issues induce important artifacts in MR images. Recently, however, a number of hurdles have been lifted, heralding new possibilities for HTS coils in MRI. In this paper, we review recent progress and challenges ahead.

First, we review the limitations of copper coils. Cryogenic RF coils become relevant when the dominant noise source in MRI is the RF coil used to collect the signal, *i.e.* in the case of nonconductive samples, or when conductive samples are probed with "small" surface antennas. With copper coils, noise reduction is readily limited by the intrinsic properties of the material. This limit can be significantly pushed by using superconductors, justifying the implementation for HTS coils in MRI with small samples or small RF coils.

We next present the progress made in the design of MRI compatible cryostats. Such cryogenic systems face the key challenges of ensuring full electromagnetic compatibility in DC and RF domains and user-friendly integration for routine practice in MR exams.

A recent study [5] has led to a much better understanding of how the static field (B_0)-inhomogeneities induced by magnetic flux expulsion in the HTS coil can be mitigated. In addition to their low intrinsic resistivity, HTS materials also present strong diamagnetism that can induce significant B_0-artifacts in MR images, such as localized signal loss and continuous phase shifts. Under the right circumstances, however, these can be avoided.

We then address the subject of the RF (B_1) coupling between the transmission coil (volume coil) and the HTS reception coil (surface coil). In the absence of magnetic coupling, the HTS coil acquires the MR signal with high sensitivity during reception and does not perturb the homogeneous RF excitation emitted by the transmission coil during transmission. This represents the targeted operational mode for HTS coils. In presence of coupling, however, the HTS coil picks up and locally amplifies the B_1^+-field generated by the transmission coil, possibly inducing important B_1^+-homogeneity artifacts in the MR images. These include large-scale signal amplitude modulations and localized π-phase shifts. To avoid the B_1^+-artifacts, a decoupling strategy must be implemented so as to deactivate the HTS coil during transmission. To illustrate this issue and its implications, this section will present the original results of an experiment implementing a decoupling strategy based on non-linearities in the RF response of the HTS material.

Finally, we discuss the perspectives for further improvements of HTS coil technology in view of novel MRI applications.

LIMITS OF COPPER COILS IN MAGNETIC RESONANCE IMAGING

Cooling the RF coil circuit at cryogenic temperatures to improve the sensitivity of nuclear magnetic resonance (NMR) detection has been an early idea [6]. From the fluctuation-dissipation theorem, the noise spectral density generated by a linear dissipative medium is proportional both to its temperature and to its power dissipation rate. A drastic reduction of the coil noise is thus expected as a result of drop of the coil resistance as the temperature is lowered. Conversely, neither the sample temperature nor its equivalent damping resistance into the coil are affected, so that the noise from the sample will eventually limit the improvement in sensitivity [7]. The earliest proofs of concept have been established with copper coils cooled to 4.2 K using liquid helium (LHe) and at 77 K with liquid nitrogen, respectively, to increase the sensitivity in ^{13}C high-resolution spectroscopy [8], and in low-field clinical MRI [9]. A dramatic improvement in sensitivity was reported in NMR spectroscopy, whereas for MRI the gain was rather modest due to the large noise induced by the human body. A few years later, the potential of HTS ceramics for replacing copper had been demonstrated with prototypes of RF coils, at 77 K for low-field MRI [10], 10 K for MR microscopy at high field [4] and 25 K for ^1H detection in a 400 MHz spectrometer [11]. Electrical losses of more than two orders of magnitude below that of copper were reported. Since these early achievements, however, the cooled-copper RF coil technology has spread widely in the markets of high-resolution NMR spectroscopy [12] and preclinical micro-MRI [13]. The replacement of copper by HTS materials, on the other hand, has remained a research topic in industrial and academic labs [3,14–18]. The objective of this section is to provide guidelines to assess the coil material performance in terms of ultimate SNR performance and report the limits achievable with copper.

Using the reciprocity principle [7], the contribution of the RF coil to the final signal-to-noise ratio in MR images can be expressed by the RF sensitivity factor S_{RF}:

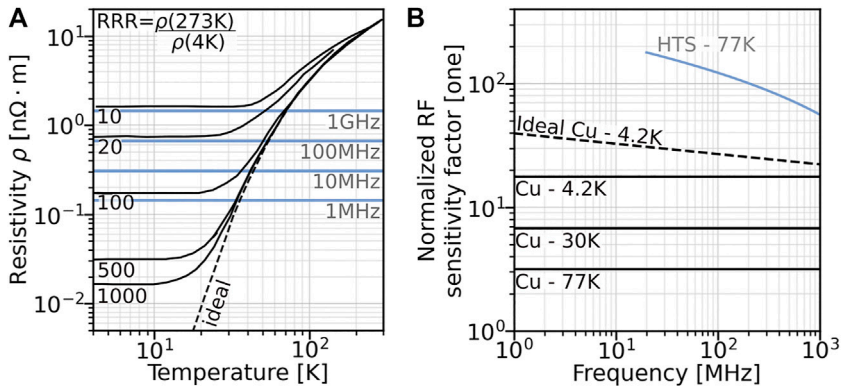

FIGURE 1 | (A) Expected resistivity ρ of copper at low temperature theoretically computed from [20], (black) and expected frontiers, i.e. $\alpha(\rho, \omega) = 1$, (blue) below which the anomalous skin effect is no longer negligible compared to the skin effect. **(B)** Corresponding RF sensitivity factor, in the case of a lossless sample, using a cooled copper coil (black) with RRR = 20 at different temperatures or a HTS coil (blue) at 77 K {data interpolated from [21]}, normalized by the sensitivity factor of the same copper coil at room temperature. The dashed line corresponds to the ultimate surface resistance achievable with absolutely pure copper, accounting for the anomalous skin effect [$\alpha(\rho, \omega) \to \infty$]. The effect of the static magnetic field on the HTS coil, not taken into account here, can significantly reduce these performances.

$$S_{RF} = \frac{\omega\left(\frac{B_1^-}{I}\right)}{\sqrt{4k_B\left(R_{\text{coil}}T_{\text{coil}} + R_{\text{sample}}T_{\text{sample}}\right)}} \tag{1}$$

that represents the time-domain SNR available from the coil per unit magnetic moment and unit acquisition bandwidth [19] at the Larmor frequency ω, assuming noiseless electronics. The RF coil circuit is modeled by a self-inductance L in series with the NMR electromotive force and with a sum of equivalent loss resistances. The term B_1^-/I, with B_1^- the transverse magnetic field amplitude generated by a RF current I in the circuit during reception, evaluates the interaction between the coil and a nuclear magnetic moment at a given position in the sample volume. The equivalent resistances R_{coil} and R_{sample} are weighted by the temperatures T_{coil} and T_{sample} to quantify the power spectral density of the noise sources in the coil and in the sample, respectively (with k_B the Boltzmann constant). By defining the quality factor Q as the ratio between the coil reactance and resistance, with respective unloaded and loaded values $Q_u = \omega L/R_{\text{coil}}$ and $Q_l = \omega L/(R_{coil} + R_{sample})$, S_{RF} is reformulated as:

$$S_{RF} = \frac{B_1^-}{I\sqrt{L}}\sqrt{\frac{\omega Q_l}{4k_B T_{eff}}} \quad with \quad T_{eff} = T_{sample}\left(1 - \frac{Q_l}{Q_u}\right) + T_{coil}\frac{Q_l}{Q_u} \tag{2}$$

where T_{eff} is the effective noise temperature of the equivalent loaded circuit. Assuming a negligible deformation of the electromagnetic field by the conduction and displacement currents inside the sample (quasistatic approximation), B_1^-/I and L do not vary significantly upon sample loading and thus only depend on the coil geometry. The measurement of Q_l and Q_u with a vector network analyzer (VNA) then allows a quick assessment of the noise sources and a comparison of sensitivity between RF coils of similar geometries operated at different temperatures and loading conditions [3].

In the case of lossless samples (i.e. when $R_{sample} \approx 0$ in **Equation 1**, or $Q_l = Q_u$ in **Equation 2**), an RF coil with a given geometry reaches an ultimate SNR performance that depends only on its temperature T_{coil} and on its resistance R_{coil}. In the following, we consider the RF regime in which the electromagnetic field only penetrates a thin layer of the conducting material. Then, R_c is directly related to the intrinsic surface resistance Ω by:

$$R_{coil} = n^2\xi\frac{a}{r}\Omega \tag{3}$$

with n the number of turns, a the average coil radius, and r the wire radius. The proximity factor ξ accounts for the concentration of the AC current along the minimum energy path in bent or parallel wires. Assuming that the term $\xi a/r$ only depends on aspect ratios of the coil geometry, then R_{coil} only depends on Ω considering homothetic scaling.

Figure 1 displays the ultimate sensitivity gain for RF coils at different cooling temperatures as compared to copper at room-temperature. For normal metals, the resistivity ρ drops almost linearly for decreasing temperatures: inelastic scattering of conduction electrons arises mainly from lattice vibrations until it reaches a temperature-independent plateau given by the residual resistance ratio (RRR) [20]. The latter is due to residual scattering by impurities and lattice defects. The screening of the metal by conduction electrons in a normal conductor leads to the RF surface resistance Ω_{nc}:

$$\Omega_{nc} = \frac{\rho}{\delta} = \sqrt{\frac{\mu_0\omega\rho}{2}} \tag{4}$$

with δ the RF skin depth and $\mu_0 = 4\pi \cdot 10^{-7}\ 4\pi\ \text{Hm}^{-1}$ the magnetic permeability of the vacuum. Actually, at extremely low ρ,Ω_{nc} can be much larger than expected from **Equation 4** because δ decreases as $\rho^{1/2}$ while the electronic mean free path λ increases as ρ^{-1} (anomalous skin effect). Since a part of the accelerated electrons tends to leave the conducting skin layer, the effective surface resistance [21] increases significantly when

$$\alpha = \frac{3}{2}\left(\frac{\lambda}{\delta}\right)^2 = \frac{3}{4}\mu_0(\rho\lambda)^2\omega\rho^{-3} \tag{5}$$

becomes comparable or greater than 1, as showcased in **Figure 1A** (grey curves). The factor $(\rho\lambda)$ is an intrinsic constant for a conductor, close to $7.2 \cdot 10^{-16}\ \Omega.\mathrm{m}^2$ for copper. When α increases well above 1,Ω_{nc} tends to a low asymptotic limit of about $3.4 \cdot 10^{-10}\omega^{2/3}$. Thus, the anomalous skin effect only affects by a few percent the data at highest frequencies of **Figure 1B**, which relies on a RRR of 20, an order of magnitude for the RRR value of copper used in MRI probes. However, due to the fast decrease of α with ρ, it represents a severe limit for copper with larger RRR values.

Figure 1B also displays the normalized RF sensitivity factor expected for a typical HTS material at 77 K. A first key feature of HTS is the partition of the conduction electrons between a coherent Cooper pair state that carries the lossless supercurrent, and a dissipative contribution from excited quasiparticle states. A second is that the electromagnetic field is extinguished over a surface layer, the thickness of which corresponds to the frequency-independent London penetration depth λ_L; in HTS, typically $\lambda_L \approx 150$ nm). The kinetic energy of the Cooper pairs is concentrated within this layer. Electrical losses are zero only for DC currents, when the Cooper pair supercurrent shorts the quasiparticle current. However, AC electric fields accelerate (and decelerate) both the Cooper pairs and the quasiparticles contained in the surface layer. Assuming that $\mu_0\omega \gg 1/2\rho_{qp}$, with ρ_{qp} the quasiparticle resistivity, the theoretical surface resistance Ω_{sc} is given by [2]:

$$\Omega_{sc} \approx \frac{1}{2}\mu_0^2\omega^2\frac{\lambda_L^3}{\rho_{qp}}. \tag{6}$$

The depth λ_L increases rapidly as the temperature or magnetic field approach the critical values T_c or H_c above which the superconducting state disappears totally. Inversely, for "perfect" superconductors, the dissipative quasiparticle contribution is supposed to progressively vanish $(\rho_{qp} \to 0)$ far below the critical limits. In HTS materials in particular, supplementary losses occur due to the motion of magnetic flux vortices, weak-link effects at grain boundaries, and the unconventional d-wave Cooper pairing mechanism, leading to complex and strongly anisotropic dependences of dissipation on the magnetic field and RF current [2]. In spite of fundamental limitations, much of the performance of a HTS material relies on its fabrication process though. For applications at 77 K, the best technology to date is that of thin-film YBCO epitaxially grown on single-crystal dielectric substrates such as lanthanum aluminate or sapphire, that exhibit extremely low tangent losses. Systematic measurements from 20 MHz to 20 GHz with temperatures between 30 and 77 K [22] show that the ω^2 dependence expected from **Equation 6** is only approached in the GHz range and is closer to a ω^1 in the low-end frequency range up to a few hundred MHz, with a typical Ω_{sc} of 0.5 μΩ at 100 MHz. Wafers of up to 20 cm in diameter are currently available from manufacturers and can be accurately etched to elaborate monolithic resonators using the substrate as capacitance. Thin-film HTS coils with quality factors from a few 1,000 to several 100,000 have been reported for MR imaging applications [19].

Another consideration with cryogenic probes comes from the thermal insulation wall inserted between the sample and the low temperature RF coil. To preserve the field-of-view accessible with the coil, the thickness of the insulator needs to be accommodated with a larger coil radius. Consequently, looking back at **Equation 1**, this tends to mitigate the sensitivity gains predicted above by reducing the B_1^-/I factor. Indeed, from the Biot-Savart volume integral and considering coils with constant aspect ratios the B_1^-/I amplitude of surface coils is expected to decrease as $1/a$ when the coil radius is adjusted to optimize the sensitivity at a target depth below the sample surface. The same $1/a$ law also applies at the center of volume coils. Considering a volume copper coil as a typical example, the ultimate SNR gain at 30 K is about seven when compared to room temperature (**Figure 1**). For a nominal sample diameter of 5 mm and a realistic thickness of 2 mm for thermal insulation, a 30 K copper coil with a mean diameter of 9 mm would thus achieve a net gain of about four over a tightly adjusted RF coil at room temperature. Coping with even smaller samples would require an improved insulation to accommodate the larger surface-to-volume ratios, which intrinsically limits the advantages of cooled RF coils over room-temperature ones below a critical sample size. Since they offer a much larger ultimate SNR performance than copper, HTS materials can significantly alleviate this limit and bring substantial SNR improvements over conventional probes even with millimetric samples [17]. More generally, far more complex rules have to be considered with large conductive samples, with a general trend to limit the SNR gain reachable with cryocooling. In any case, however, HTS materials that provide much lower losses than their copper counterparts offer a promising perspective to design novel RF coil geometries such as actively screened or meta-structured configurations.

PROGRESS IN MAGNETIC RESONANCE IMAGING COMPATIBLE CRYOSTATS

The need for cryogenic means has long been seen as a serious bottleneck to the dissemination of cooled RF coil technology in MR applications. Many advances have been made during the last 20 years in the emerging field of superconductive electronics where the requirement for low-cost, compact, secure, and easy-to-use cryogenic devices has been a strong motivation [23]. However, MR detection meets severe additional constraints of compatibility with the presence of RF as well as of large static magnetic fields: no metallic parts can be present near the RF coil and no magnetic materials nor moving metallic parts can be in proximity to the magnet bore. Specific materials such as PVC, fiberglass composites, polystyrene or polyurethane foams, quartz, glass, or ceramics are generally involved in the cryostat body. Thus, initial developments [19] mostly relied on homemade cryogenic designs. First trials involved immersion of the coil circuit in LHe (4.2 K) or LN_2 (77 K) [8,9], allowing intrinsically uniform and temperature-stabilized cooling of volume coils or large surface coils. To reduce mechanical and electrical instabilities due to boil-off and bubbling, the trend was then to replace the direct liquid immersion by a flow of cold

nitrogen [24] or helium [25] gas, or by a cold finger made of high-performance dielectric material such as sapphire [11,26].

Another particular constraint that arises during the study of human subjects, animal models and biological samples is to maintain the living system at room temperature all the while keeping a small separation from the cooled RF coil. This can be provided either by a plain insulating wall [10], by a double-wall vacuum layer [25], or by a single-wall evacuated cryostat containing the RF coil [27]. The latter allowed the reduction of the insulator thickness to less than 1 mm, which is particularly suitable for high-resolution surface imaging such as that of the human skin and rodents in a preclinical setting. Nevertheless, using conventional superinsulation with metallized layers to block thermal radiation through the insulating window does not fit the requirement for RF transparency, so an amount of thermal leakage still occurs. Thus, insufflation of a warm stream of an inert gas such as N_2 into a reserved space along the outer cryostat surface has been applied to preserve the temperature stability of small living samples [24]. As pointed out in the previous section, the requirement for a minimized insulation thickness is not as severe with HTS coils as with copper coils since the formers offer much higher ultimate SNR gains.

More than 15 years after the early demonstrations of RF coils cooled by direct fluid immersion in the academic world, more elaborated closed-cycle cooled RF probes [28] have become available as standard accessories for analytical NMR spectroscopy [29]. In the new probes, typically, circulating helium gas transfers the cooling power from a distant two-stage Gifford–McMahon refrigerator to the RF coil, through heat exchangers at a regulated temperature ranging between 20 and 30 K. Temperatures of 20–30 K are low enough to improve the sensitivity of copper RF probes by a ratio of four when compared to room temperature, which enables 16 times faster acquisitions at constant SNR. Moreover, an integrated preamplifier cooled to below 80 K by the first stage of the Gifford-McMahon machine ensures a low noise contribution from the receiver, even with noiseless samples. Such new technology has been expanding rapidly since the late 1990s to face the high throughput demand in analytical chemistry. Its impact is tremendous in large scientific domains such as genomics, proteomics, and drug discovery, where the structural and dynamic analysis of large proteins is very time consuming, only small amounts of the substance under study are available, and less sensitive nuclei such as ^{13}C and ^{15}N must be investigated [12].

Based on the closed-cycle technology already developed for NMR probes, cryocooled surface probes designed for high-resolution imaging of the mouse brain [30–32] have become commercially available for routine operation on micro-MRI systems up to 15.2 T. This has given rise to growing numbers of cutting-edge structural and functional imaging applications [13]. Typically, the probes are made of 15–20 mm circular or rectangular copper coil elements bent onto a cold finger. Their half-cylindrical shell packaging leaves a large access to the animal head and offers a warm contact with a temperature-controlled ceramic wall, ensuring a minimum coil-sample distance of about 1 mm. Compared to a similar probe operating at room temperature, *in vivo* image acquisition with a 30 K quadrature surface probe at 9.4 T exhibited a SNR gain of about 2.5 when averaged over the mouse brain [31].

The rather high temperature range targeted with the new closed-cycle technology allows a much more robust operation than achievable with the early cryostats operating at 10 K and below. Notably, the new technology offers a fully automated control and does not require to refill the system with cryogenic fluids. However, designs until now were not versatile enough to allow for a change of RF coil configuration or orientation. The set-up is expensive and cumbersome because a high cooling power is required from the Gifford-McMahon unit, the rotary valve of which has to be located a few meters away from the MRI magnet for electromagnetic compatibility issues. Moreover, while cooling to 30 K is needed to take the most out of copper RF coils, HTS materials already exhibit sufficient performances at temperatures above 50 K. Thus, research activity is still ongoing in academic labs with simple all-in-bore 77 K static cryostats offering some flexibility and sufficient autonomy for acquisition times of several hours [3,33–36].

In order to optimize the handling of HTS coils, cryogenic systems providing intermediate temperature control above 50 K [15,37–40], and variable temperature set-ups for frequency tuning [39,41] have been proposed. Along with a higher working temperature, an important trend to alleviate the charge on closed-cycle cryocoolers is to drastically reduce the distance between the refrigerator machine and the cooled RF coil. Pulsed tube refrigerators without moving parts close to the cold finger have been used at close proximity to the MRI magnet, i.e. on the patient bed [42], or even inside the magnet within the RF coil cryostat [37]. The latter solution was designed to allow a variable orientation of the RF coil with a very compact design; however, it actually needs to be operated in a downward orientation (i.e. upright for the pulse tube) because of gravity issues for ensuring an efficient flow cooling.

The use of a refrigerant was eliminated in the cryogen-free system proposed by [40], later described by [42], and displayed in **Figure 2**. The cold source, provided by a commercial single-stage pulse tube cryocooler connected to a remote motor, is located directly on the non-magnetic cryostat vessel. The cold head is thermally coupled to the HTS coil by a series of high-conductivity pure aluminum flexible straps used in combination with copper and sapphire supports, as depicted in **Figure 2B**. This solution allows the transfer of sufficient cooling power to the RF coil; offers great adaptability to the RF coil bedding geometry; minimizes static and RF magnetic field perturbations induced by the system; and minimizes the transfer of mechanical vibrations to the HTS coil. Moreover, a non-magnetic heat exchanger tip anchored to the coil bed and a fully automated control system enable the control of the coil temperature to within 0.1 K, [41,42]. Thus, the coil frequency can be tuned through temperature as a parameter. These aforementioned characteristics, as well as the reasonable weight (70 kg) and compact nature of the cryostat, allow an installation as close as possible to the measurement zone of the MRI scanner. In fact, this system is cryogenist-free—i.e. no cryogenic knowledge is required to use it -, autonomous, and adaptable to any MRI structure that stays in the examination room during the experiments.

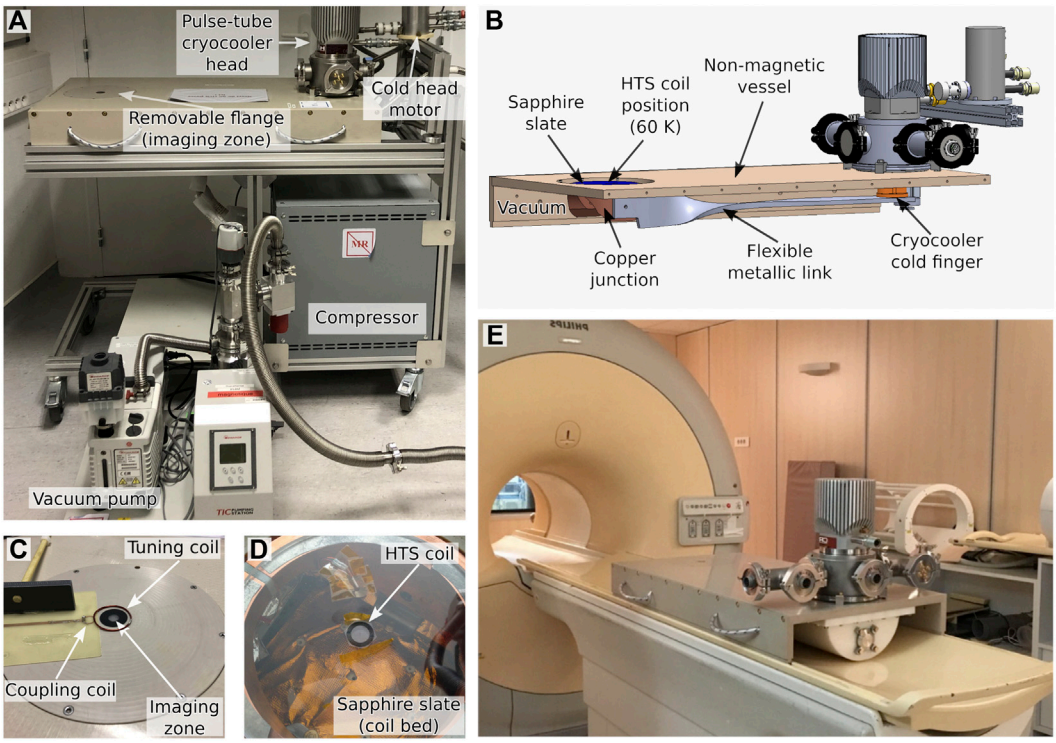

FIGURE 2 | Images of the cryogen-free cryostat. **(A)** The cryostat and associated equipment. **(B)** Detailed 3D drawing of the general layout and cryogenic scheme of the system. **(C)** The HTS coil signal is probed by inductive coupling via the coupling coil. Matching and tuning of the HTS coil to the acquisition chain of the MRI scanner is performed with the coupling coil and the tuning coil, respectively. Fine tuning is also achieved via temperature control of the HTS coil. **(D)** Position of the HTS coil inside the cryostat, approximately 1.7 mm under the imaging zone. **(E)** Cryostat on the patient bed which can be inserted in the bore of the 1.5 T MRI scanner. This system was fully described in [42].

MITIGATING THE EFFECTS OF HIGH-TEMPERATURE SUPERCONDUCTING COIL DIAMAGNETISM

Another recent advance was made by better understanding the interaction between the HTS coil and the static magnetic field B_0 used in MRI. In the presence of a magnetic field, superconductors spontaneously generate screening currents on their edges and surfaces to expel the magnetic flux. This induces static field (B_0)-inhomogeneities in the vicinity of the superconductor, which can result in B_0-artifacts in the MR images. In type-II superconductors, which include all HTS materials, magnetic flux can be readmitted in the form of quantized flux lines, or "vortices" [43]. Consequently, the magnetic properties of HTS materials are typically temperature dependent and hysteretic. Depending on the magnetic history of the material, notably whether it was cooled in the presence (field cooled) or the absence (zero-field cooled) of a magnetic field, it can display perfect or imperfect diamagnetism. As presented in the previous section, HTS coils for MRI applications have mostly been used at LN_2 temperature, i.e. sufficiently close to the superconducting transition temperature T_c of the HTS material for its diamagnetism to be negligible. However, with better-controlled experimental parameters and new cryostats achieving lower temperatures (~ 60 K) this becomes an issue producing major B_0-artifacts on MR images in the vicinity of the HTS coil.

The static field inhomogeneity artifacts due to static field expulsion from HTS coil were recently investigated [5] for different cooling conditions and temperatures of the HTS coil. This was done by measuring the MR signal at 1.5 T of a water sample in the vicinity of a HTS coil: a 12 mm multi-turn Transmission Line Resonator [44] (MTLR) with a pair of six-turn YBCO spirals (T_c = 86 K) on both sides of a Al_2O_3 substrate. In the aforementioned study, the HTS coil was non-resonant to avoid RF B_1^+-artifacts while keeping intact the diamagnetic response of the superconductor. The coil was used in the cryostat described in **Figure 2**, and the normal to its surface was kept perpendicular to the static field B_0 during the whole experiment. A whole-body RF coil was used in transceiver mode. Standard 3D gradient-echo MR images were acquired after zero-field cooling (outside the MRI scanner), field cooling (inside the MRI scanner) and for different temperatures varying from 60 to 90 K.

In **Figure 3**, we present the main results of this study. Images acquired after zero-field cooling displayed important signal losses and phase perturbations (**Figure 3A**). The observed artifacts were predominant closer to the HTS coil and shared the same

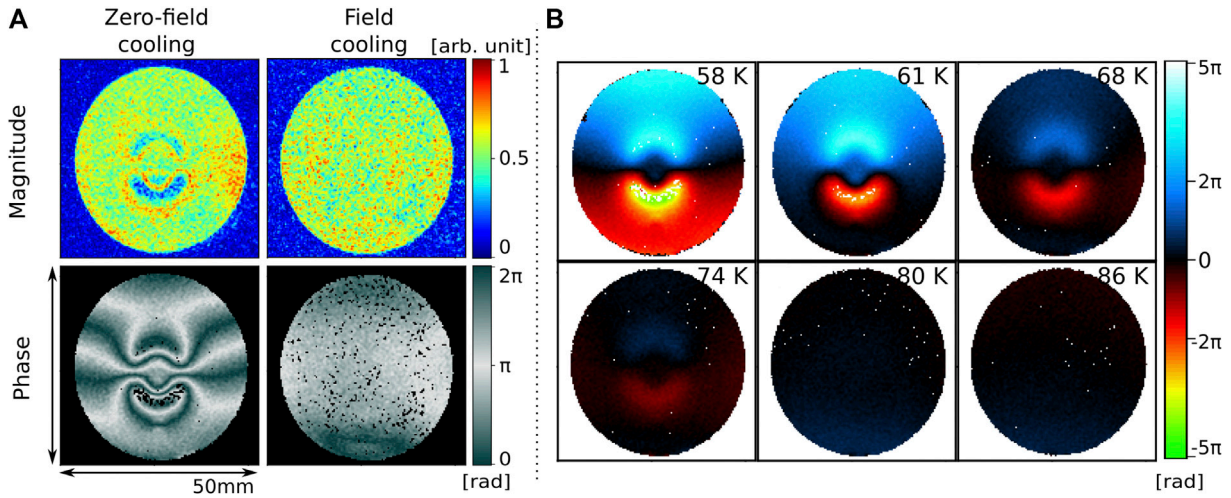

FIGURE 3 | MR images of a water sample in the vicinity of a HTS coil **(A)** after different cooling conditions of the coil (at 58 K), and **(B)** for different temperatures of the coil after zero-field cooling. The slice shown is parallel to the HTS coil plane, ~4.2 mm above. $\vec{B}_0$ is oriented towards the vertical axis of the images. In **(B)**, the phase data were unwrapped, resolving the 2π-jumps. Data taken from [5].

characteristic dimensions. In comparison, images acquired after field-cooling the coil in the MR scanner were unaltered. The phase perturbation was also shown to have a strong temperature dependence (**Figure 3B**); the amplitude of the perturbation was continuously reduced as the temperature increased. Using a phenomenological model of the coil superconducting diamagnetism, it was shown that these artifacts were caused by a small yet unavoidable misalignment, less than 1°, of the HTS coil in the static field B_0, and that their temperature dependence mirrored the temperature dependence of the in-plane critical current of YBCO measured in comparable conditions [45].

Two important conclusions can be drawn from these results. 1) The B_0-artifacts are linked to a low working temperature of the coil when compared to its T_c, and 2) they can be mitigated at low temperature by field-cooling the HTS coil in B_0 at its working position in the MRI scanner.

DECOUPLING THE HIGH-TEMPERATURE SUPERCONDUCTING COIL DURING TRANSMISSION

Another possible source of artifacts comes from the magnetic coupling between the HTS surface coil and the volume coil used during transmission. Copper coil technology typically relies on diodes to deactivate the reception coil during transmission. Unfortunately, these standard techniques cannot be implemented with HTS materials, as the physical connections required for incorporating discrete components in the coil circuit degrade its quality factor and add too much noise. Decoupling is hence a major technological challenge for HTS coils. A solution can be found through the highly nonlinear electrical properties presented by HTS materials [46]. The quality factor Q of HTS coils depends on the power of the incident RF magnetic signal. Their Q of a few thousand during reception (low power stage), typically collapses to a few dozen during transmission (high power stage) [47,48]. These nonlinear properties, which can be tailored by fine engineering of the superconducting track composing the coil, can be exploited as a means to deactivate the HTS coil during transmission [49]. Here we present a study of these nonlinear properties. In a first step **(Setup 1)**, we will present results of a RF characterization of a HTS coil realized in a low field environment (Earth magnetic field). These results will provide insight into the physical mechanism behind the

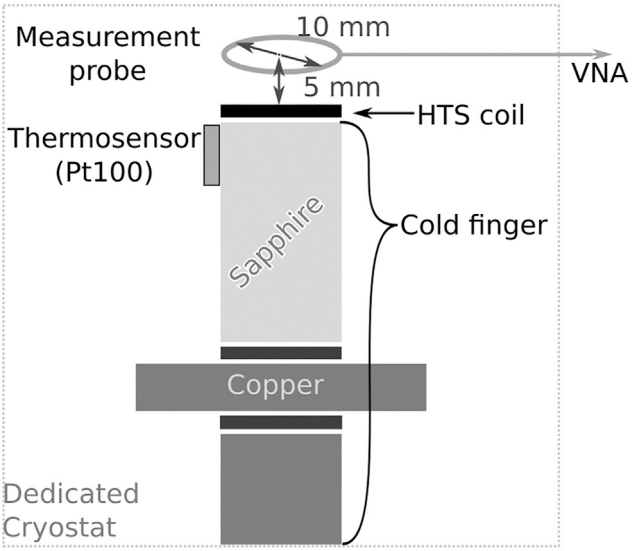

FIGURE 4 | Schematic drawing of the interior of the dedicated cryostat used in Setup 1.The VNA is connected to a measurement probe inductively coupled to the HTS coil, which is secured on a cold finger. The temperature is monitored using a thermosensor (Pt100). The system was fully described by [50].

TABLE 1 | Acquisition parameters of the 3D gradient-echo MRI sequence used in Setup 2.

	HTS coil	Copper coil (Reference)
Pixel receiver bandwidth	217 Hz/pixel	217 Hz/pixel
Echo time/Repetition time	6 ms/25 ms	3 ms/13 ms
Spatial resolution	250 μm × 250 μ × 250 μm	300 μm × 300 μm × 1,000 μm
Field of view	36 mm × 36 mm × 36 mm	20 mm × 20 mm × 20 mm

collapse of the coil quality factor Q. In a second step **(Setup 2)**, we present this decoupling approach implemented in an MRI environment (**Figure 2**), allowing the material to pass from a zero-resistance state to a dissipative state during transmission [49]. In both setups, the experiments were conducted with a resonating (ω = 63.5 MHz at 70 K) HTS surface coil of identical design as the one described in the previous section [5].

Setup 1—The HTS surface coil is used in a dedicated cryostat [50] shown schematically in **Figure 4**, cooled in Earth's magnetic field and characterized with a VNA and a method inspired from [47]. The electrical parameters of the HTS coil are obtained through the measurement of its RF response using an inductive coupling approach involving a measurement probe overcoupled with the HTS coil. The measurement probe is a 10 mm diameter copper loop placed in front of the HTS coil at a 5 mm distance. The incident power produced by the VNA and transmitted to the HTS coil *via* the measurement probe is then converted in equivalent B_1^+ or B_1^- values, depending on the RF amplitude with this experimental geometry. The HTS coil was left resonating at its own resonant frequency, different from the Larmor frequency, for the experiments involving Setup 1.

First, this setup simulates an MRI sequence. A high amplitude pulse with $B_1^+ \in [0.02\,\mu T, 0.4\,\mu T]$ is applied with the measurement probe to mimic the RF pulse used during spin excitation (transmission). Then, a low amplitude pulse corresponding to $B_1^- = 0.02\,\mu T$ is applied to reproduce the NMR signal during reception. The switch time between the two power levels is 12 μs. The HTS coil quality factor Q was extracted as a function of B_1^+ (during the excitation pulse) for three temperatures T = 60, 70, and 80 K.

Secondly, the setup performs a swept-frequency analysis where the modulus and phase of the compensated reflection coefficient $\rho_{comp}(\omega)=\rho(\omega)-\rho_0(\omega)$, are measured with the VNA as a function of the frequency ω for different incident $B_1^+ \in [0.05\,\mu T, 0.35\,\mu T]$ and temperatures T = 60, 70 and 80 K. Here, ρ_0 corresponds to a reference data set taken in the absence of the HTS coil, whereas ρ integrates its contribution [47].

Setup 2—Then, the HTS coil is cooled inside the MR compatible cryostat [42] integrated into a 1.5 T clinical MRI (Achieva, Philips) shown in **Figure 2**. Fine frequency tuning of the HTS coil at ω_0 is performed using a tuning coil [3], while impedance matching is obtained with a coupling coil (**Figure 2D**). The same coupling coil is then used to pick up the HTS coil signal during the experiment. The MRI sequence is a standard 3D gradient-echo using the parameters listed in **Table 1**. During transmission, a volume (whole-body) coil is used to generate rectangular RF pulses with nominal amplitude $B_1^+ \in [0.08, 27\,\mu T]$ and pulse durations $t \in [6.4\,\mu s, 4.0\,ms]$. The pulse duration τ is calculated consequently to keep the flip angle constant ($\alpha = \gamma B_1^+ \tau$). Also, the imaging sample (**Figure 5A**) is filled with a 1 ml solution of water with a gadolinium-based contrast agent (Dotarem, $C = 2.5 \cdot 10^{-3}$ mmol/ml).

With this second setup, we first connected the coupling coil to the MRI acquisition RF channel to acquire the HTS coil signal during reception. A reference measurement was obtained using a room temperature copper coil of similar dimensions (**Figure 5A**). Then, the imaging sample was removed and the coupling coil signal V was connected to an oscilloscope to measure the response of the HTS coil during transmission as a function of B_1^+ at different temperatures $T \in [62\,K, 80\,K]$. A reference measurement was also acquired with the coupling coil only (i.e. without the HTS coil). The ratio V/B_1^+ was then used to track the evolution of the HTS coil quality factor Q. In addition to these measurements, the quality factor Q of the HTS coil was also measured in this configuration using a VNA and an incident power producing a $B_1^+ \sim 0.05\,\mu T$.

Figure 6 presents the results obtained with Setup 1. **Figure 6A** displays the dependance between the Q value of the HTS coil and B_1^+ for three working temperatures of 60, 70 and 80 K. We observe a transition from a superconducting state ($Q \sim 50000$) to a dissipative state ($Q \sim 100$) for B_1^+ values that are temperature dependent. At lower temperature (60 and 70 K), this transition occurs at $B_1^+ \sim 0.2\,\mu T$ whereas at 80 K (closer to T_c), B_1^+ is reduced by almost an order of magnitude to 0.04 μT. Also, we mention that the transition time (not shown here) between the two states was faster than 12 μs.

The effects of the RF power on the HTS material are shown in **Figures 6B–G**, which displays the modulus and phase of ρ_{comp}, noted respectively $|\rho|$ and ϕ thereafter, for different incident B_1^+ and working temperatures. First, at low B_1^+, $|\rho|$ and ϕ display the expected behavior for classical RF coils, except for the temperature dependence of the resonance frequency; at 60 and 70 K, the coil resonates close to 63.5 MHz, which decreases to 63.1 MHz at 80 K. This frequency shift, which is due to the temperature-induced increase of the kinetic inductance of the superconductor, is predominant when T_c = 86 K is approached. Secondly, at higher B_1^+, we observe a collapse of $|\rho|$ and a deformation of ϕ that are also temperature dependent. At 80 K, $|\rho|$ and ϕ simply flatten as B_1^+ increases. This is to be compared with the behaviour observed at 60 and 70 K, where $|\rho|$ becomes strongly deformed at $B_1^+ = 0.35\,\mu T$ and ϕ showcases a discontinuity (inset of **Figures 6C,E**).

In **Figure 5**, we present the results acquired with Setup 2. The spatial inhomogeneities observed in the MR images of **Figures 5B–C** are due to a non-uniform flip angle of the spins over the

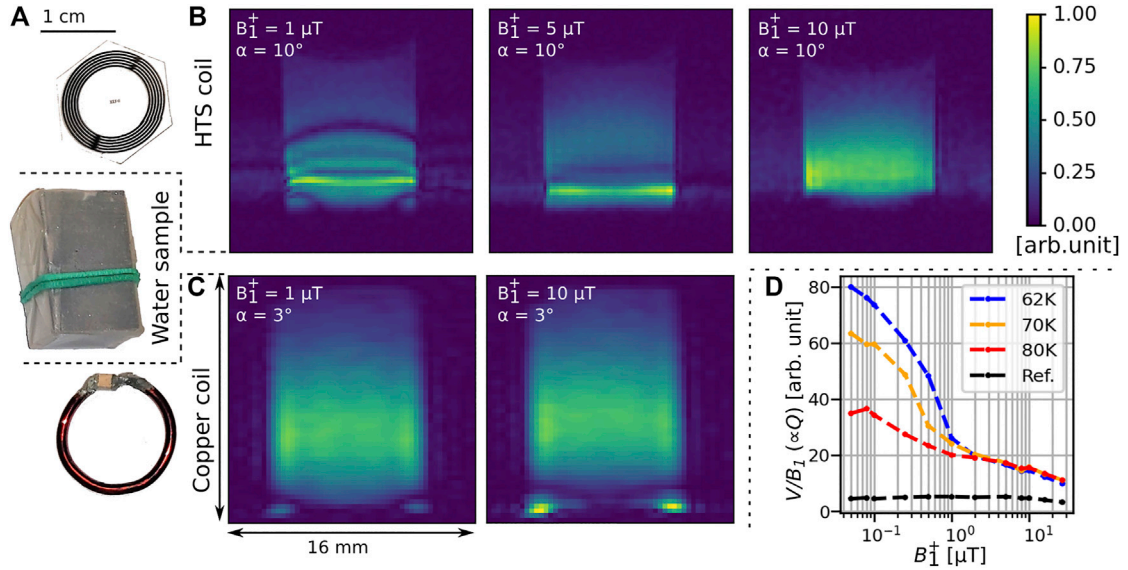

FIGURE 5 | (Setup 2)–**(A)** Pictures of the HTS coil, water sample and copper coil. MR acquisitions obtained with **(A)** the HTS coil at 60 K and **(B)** the copper coil at room temperature for different B_1 varying from 1 to 10 µT at constant spin flip angle α. **(C)** V/B_1^+ ratios ($\propto Q$) as a function of the RF magnetic field B_1^+ transmitted by the volume coil.

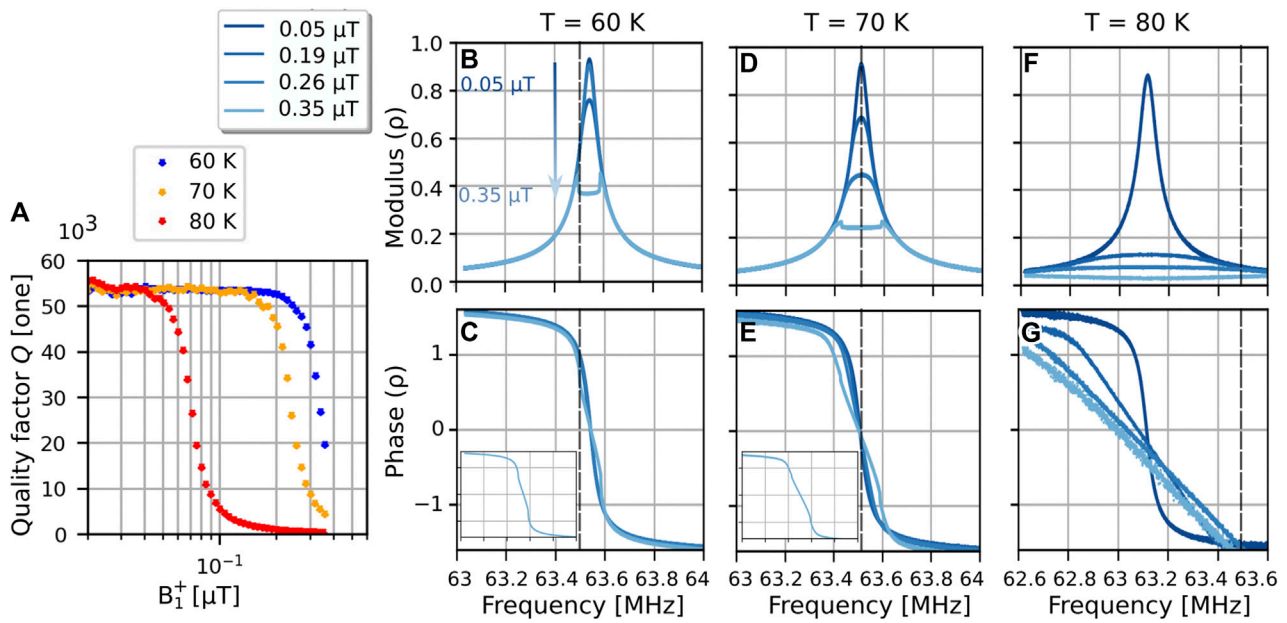

FIGURE 6 | (Setup 1)–**(A)** Measured quality factor Q of the HTS coil as a function of the RF magnetic field B_1 for different temperatures and **(B–G)** swept-frequency analysis of the nonlinear HTS coil for different temperatures and B_1. The top **(B,D,F)** and bottom **(C,E,G)** rows respectively display the modulus and phase of the compensated reflection coefficient ρ_{comp}. The dashed line at 63.5 MHz provides a visual guideline to highlight the temperature drift of the resonance frequency. The insets in **(C)** and **(E)** highlight the phase discontinuity observed for B_1 = 0.35 µT.

sample. This is produced during transmission by the re-emission of the spatially non-uniform B_1^+ field generated by the surface coil, the amplitude of which is proportional to its quality factor Q. In the absence of artifacts, the MR signal would appear relatively uniform over the sample. For a copper coil presenting linear electrical properties (**Figure 5C**), the magnitude of the artifacts does not depend on the value of B_1, as expected at a given flip angle α. For the HTS coil, however, the artifacts in **Figure 5B** are more important at lower B_1^+. This indicates that increasing B_1^+ increases the resistance of the coil, and consequently reduces its quality factor Q during transmission. This behaviour is well observed when we measure the signal of the coupling coil

during transmission. As shown in **Figure 5D**, the ratio V/B_1^+, which is proportional to Q, decreases as a function of B_1^+ of almost one order of magnitude between 0.05 and 10 μT at 62 K. In comparison, this coefficient is almost constant for all B_1^+ values without the HTS coil (ref. curve in black on **Figure 5D**). For values of B_1^+ below 1 μT, Q displays a strong temperature dependence, which is not the case anymore for higher B_1^+. This dependence was also observed with the Q measurement of the HTS coil inside the magnet performed with the VNA, typically with $Q \sim 3000$ at 60 K and $Q \sim 2560$ at 70 K.

These two setups studied the nonlinear electrical properties of the HTS coil in Earth's magnetic field (Setup 1) and in a field of 1.5 T (Setup 2). We observed differences between the behavior of Q in Earth's field and at 1.5 T, in agreement with a previous study (Lambert RSI 2008). This difference can be explained by vortex dynamics, which we assume to be the principal dissipation mechanism in our experiment [51]. The AC current circulating in the HTS coil, depending on $(B_1^+)^2$, is responsible for energy dissipation in the HTS material and leads to the increase of its electrical resistivity (i.e. its surface impedance). In Earth's field, vortex penetration is weak and does not, unless the temperature closely approaches T_c, affect the HTS material response much. At low B_1^+, the vortices remain pinned and the RF current is not strong enough to induce large vortex displacements. Consequently, the surface impedance of the coil remains constant, leading to $Q \approx 50000$ for all working temperatures, in good agreement with precedent measurements {Lambert RSI 2008 [3]}. At higher B_1^+, the effect of hysteretic vortex motion in the HTS material becomes significant, inducing an increase of the electrical resistance, and a decrease of the Q values that amounts to one order of magnitude between 60 and 70 K. This is even more pronounced with an increase of temperature: we observe a decrease of two orders of magnitude of Q. At 1.5 T, the critical current density is lower, and the vortices are more easily set in motion by RF currents even at low B_1^+. This phenomenon becomes more pronounced as the temperature of the HTS material is increased. Consequently, Q is halved between 60 and 80 K. In contrast, for $B_1^+ \geq 1$ μT, Q does not depend on the temperature anymore. This is most probably due to a complete penetration of the material by the vortex lines carrying B_1^+; once the RF field completely penetrates the material, there is no further change in field contrast associated with B_1^+, so that all related artifacts are now independent of temperature. In the experimental results, we observed that the value of B_1^+ at which the superconducting material transits from the superconducting state to the dissipative state depends on temperature, but also on the value of the static field. This can be explained by the temperature, field, and field-orientation dependence of the critical current density of the HTS material, as studied by [45], in comparable conditions.

DISCUSSION

In this work, we reviewed some of the challenges and recent advances made in the implementation of HTS coil in MRI. The key feature of HTS coils is that they do not share the lower limit on resistivity experienced by copper coils, although the ω^2 proportionality law between their electrical noise and working frequency limits their potential for applications in high-field MRI. HTS coils do, however, share the same extrinsic limitations as cryogenic copper coils. To take full advantage of their benefits, the necessity for the sample to be non-conductive, or at least not to overload the coil (c.f. **Equation 2**), restrains the imaging volume to small dimensions for *in vivo* applications at standard medical imaging fields (i.e. up to a few milliliters at 1.5 and 3 T), as discussed in the literature [19]. As for cryogenic copper coils, this limits the prospects of implementations of HTS coils as volume coils. For larger samples, they could nevertheless be implemented as coil arrays, which would allow HTS coils to image far greater fields-of-view while keeping advantageous SNRs. The issue of decoupling the array elements from each other entails substantial work, but a solution could be based on the work of [52], or that of [14]. Considering the small dimensions of HTS coils, they could only be used for surface imaging in clinical MRI for skin [53] or extremities imaging, for instance. In preclinical MRI, they will probably come as a natural successor to cryogenic copper coils, as they are well suited for weakly conductive small biological samples such as mice and rats, or *ex-vivo* biological samples [54]. The high sensitivity of HTS coils also opens up the way to high-resolution MRI (<100 μm) at relatively low fields (<3 T) when compared to the more usual high fields used in preclinical MRI (4.7 T and higher). Since the MR relaxation times depend on B_0, there is a strong motivation to investigate animal models directly in clinical magnetic fields, since this approach greatly facilitates the transfer of MR protocols from preclinical to clinical imaging. Hence, this limits the need for additional investments.

In order for these applications to be developed, the HTS coil must be integrated into a cryostat that achieves both MRI compatibility and good thermal insulation between the cryogenic probe and the room temperature imaging subject. Although this has proven to be an important technological challenge, recent years have seen the design of new and more robust cryostats, with the notable development of the cryogen-free and autonomous system that we described [42]. While we focused our attention primarily on closed-cycle technology, onboard open-cycle cooling approaches dedicated to small RF coils show promising perspectives to address the challenge of cooling high-density flexible HTS coil arrays, i.e. arrays where the relative positions of the coil elements can be modified. Such individual onboard cooling units or, alternatively, distributed refrigerant streams, could be implemented respectively with a compact N_2 Joule-Thomson refrigerator [55] or a microfluidic LN_2 exchanger [56]. The actual challenges of such a device are improving the compactness and reducing the cooling time while keeping a standalone, user-friendly, and cryogen-free solution. Compactness will be achieved by reducing the dimensions, and therefore the weight of the device. Consequently, this will reduce the heat stored in the system at room temperature as well as the thermal resistance between the cooling system and the coil, allowing for faster cooling or less cooling power. This cannot be accomplished without a fine optimization of the thermal capacity of the thermal link with the cooling power of the cryocooler at all stages of cooling. These improvements will

bring the device even closer to the MRI measurement zone and impose having even more non-magnetic material entering its composition. Using new polymeric materials—robust, lighter, and compatible with vacuum and MRI scanners–, will fulfill both requirements.

The question of the optimal working temperature for HTS coils remains open. On the one hand, we have seen that working at temperatures significantly lower than T_c may be associated with circumstantial static field inhomogeneity artifacts caused by the superconducting diamagnetism of the coil; these could be avoided by field cooling the coil in the MRI magnet at its working position. On the other hand, working at lower temperatures should lead to a better sensitivity factor (S_{RF}) of the HTS coil. Therefore, regarding superconducting diamagnetism, working at a lower temperature can be envisioned if these artifacts are consistently avoided. For most applications, this implies frequent temperature cycling of the coil in-between experiments or after a change in geometry. This requires a practical implementation involving quick, localized and uniform heating of the HTS coil inside the cryostat. Such a heating system could work by radiative, resistive, or conductive heating but without any interference with the MRI experiment, and would solve an important issue in the implementation of HTS coils by providing the experimental conditions required to obtain better images with this technology.

The issue of tuning and decoupling of the HTS coil also comes into play for the selection of its working temperature. Until now, our studies were conducted using HTS coils working at around 80 K in transceiver mode. As stated earlier, the HTS coil design is chosen so as to resonate close to the Larmor frequency, and a fine tuning of its resonance frequency is achieved by positioning a closed-circuit copper loop [3]. Thanks to the new cryostat, this fine tuning can now be performed by a fine control of the temperature, as proposed by [42], since the coil resonance frequency depends on the temperature [39]. Also, matching the HTS coil to the source impedance was achieved by a contactless matching technique using an inductive pick-up loop tuned at the Larmor frequency. The coupling coefficient is manually adjusted, modifying the distance between the pick-up loop and the HTS coil, to reach the optimal 50 Ω presented at the input preamplifier. This matching step can be made more user-friendly by the integration of an automated system based on piezoelectric motors inside the cryostat [57].

In parallel, until the issue of the magnetic coupling between the HTS coil and the transmission volume coil is solved, the former can still be used in transceiver mode (i.e. as the transmitter and receiver) Typically, the transmit level of the coupled volume coil is manually adjusted to account for the presence of the HTS coil, which effectively becomes the source of the RF excitation flipping the sample magnetization during transmission. From the perspective of the volume coil, this leads to flip angle values of one to two orders of magnitude smaller than the ones currently used in MR protocols in order to achieve a real π/2-flip angle in the region of interest (ROI) These precautions are necessary to limit the B_1^+-artifacts caused by the HTS coil non-uniform magnetic field. Although this corresponds to a suboptimal implementation of HTS coil, high quality MR images can still be obtained in this operational mode [3]. However, the presented investigations were all based on gradient-echo protocols, and imaging a larger area was realized at the cost of a nonuniformly weighted T1 contrast. Many of the sequences requiring a uniform flip angle to assess a quantitative T1 or T2 contrast, for instance, are not usable in this condition. Consequently, achieving decoupling with HTS coil will open up a new world of applications for this technology.

To that end, the approach illustrated in our experimental results exploits the non-linear electrical response of HTS materials to minimize the quality factor during transmission. Although the coil under study did not reach resistance levels sufficient to achieve proper decoupling, it did provide a proof of concept for this technique. To go further, the HTS coil have to reach its dissipative state for lower RF B_1^+ field values which implies finding ways for the coil current to reach the critical current density of the HTS material sooner. This must be accomplished without degrading the coil sensitivity during reception. This objective can be achieved either by reducing the critical current density notably through temperature, as seen in **Figure 5** and providing another argument for working at higher temperature, or by increasing the current density in the coil by a fine engineering of the superconducting track [49]. This can be performed by adding constrictions of various geometries in the coil design and modifying the HTS material thickness.

CONCLUSION

HTS coil for MRI has come a long way in the last 30 years. Cryogenics have advanced sufficiently to allow the design of MRI compatible cryostats that allow one to reliably operate HTS coils. In addition, we now better understand how HTS coils interact with the superposed magnetic fields B_0 and B_1 used in MRI, allowing for a better integration of the superconducting coil in the MR environment. This technology still faces several challenges before it is ready for practical applications in bio-imaging. However, the significant increase in sensitivity it offers lends it the prospect of being ultimately disruptive.

DATA AVAILABILITY STATEMENT

The raw data supporting the conclusion of this article will be made available by the authors, without undue reservation.

AUTHOR CONTRIBUTIONS

AL: coordinated the writing of the paper; was involved in the redaction of many sections of the article; and acquired parts of the data shown. GA and BB: designed the MRI compatible cryostat shown in the paper; and both were involved in the writing of the section "Progress in MRI compatible cryostats" which displays their work. JB and CvdB: helped design the experiment—Setup 2—shown in the paper; were involved in the writing of the section "Decoupling the HTS coil during transmission;" provided expertise during the discussion of the experimental results LD:

wrote the state-of-the-art sections for "Limits of copper coils in MRI" and "Progress in MRI compatible cryostats" MPQ: coordinated the research project; involved in the design of the experiments shown in this work; main writer of the section "Decoupling the HTS coil during transmission." All authors actively contributed to the writing of this paper.

FUNDING

Experiments were performed on the 1.5 T MRI platform of CEA/SHFJ, affiliated to the France Life Imaging network and partially funded by the network (Grant ANR-11-INBS-0006), under Grant No. ANR-14-CE17-0003 (SupraSense project) and LabeX LaSIPS (ANR-10-LABX-0040-LaSIPS).

ACKNOWLEDGMENTS

The authors thank Dr. Jean-Christophe Ginefri for his contribution to the development of HTS coils within our research group. The authors also thank Rose-Marie Dubuisson for her help with the 1.5 T MRI scanner platform, and Georges Willoquet for his work on the electronics implemented in both cryostats used in this work, as well as Isabelle Saniour and Michel Geahel for their past contributions to this project.

REFERENCES

1. Bednorz JG, and Müller KA (1986) Possible highT C Superconductivity in the Ba-La-Cu-O System. *Z für B - Condens Matter* 64, 189–93. doi:10.1007/BF01303701
2. Lancaster MJ (1997, Passive Microwave Device Applications of High-Temperature Superconductors). *Passive Microwave Device Applications of High-Temperature Superconductors*. United Kingdom: Cambridge University Press doi:10.1017/CBO9780511526688
3. Poirier-Quinot M, Ginefri J-C, Girard O, Robert P, and Darrasse L (2008) Performance of a Miniature High-Temperature Superconducting (HTS) Surface Coil for *In Vivo* Microimaging of the Mouse in a Standard 1.5T Clinical Whole-Body Scanner. *Magn Reson Med* 60, 917–27. doi:10.1002/mrm.21605
4. Black RD, Roemer PB, Mogro-Campero A, Turner LG, and Rohling KW (1993) High Temperature Superconducting Resonator for Use in Nuclear Magnetic Resonance Microscopy. *Appl Phys Lett* 62, 771–3. doi:10.1063/1.108574
5. Labbé A, Dubuisson R-M, Ginefri J-C, Van Der Beek CJ, Darrasse L, and Poirier-Quinot M (2020) Static Field Homogeneity Artifacts Due to Magnetic Flux Expulsion by HTS Coils for High-Resolution Magnetic Resonance Imaging. *Appl Phys Lett* 117, 254101. doi:10.1063/5.0033894
6. Hoult DI, and Richards RE (1976) The Signal-To-Noise Ratio of the Nuclear Magnetic Resonance experiment. *J Magn Reson (1969)* 24, 71–85. doi:10.1016/0022-2364(76)90233-X
7. Hoult DI, and Lauterbur PC (1979) The Sensitivity of the Zeugmatographic experiment Involving Human Samples. *J Magn Reson (1969)* 34, 425–33. doi:10.1016/0022-2364(79)90019-2
8. Styles P, Soffe NF, Scott CA, Crag DA, Row F, White DJ, et al. (1984) A High-Resolution NMR Probe in Which the Coil and Preamplifier Are Cooled with Liquid Helium. *J Magn Reson (1969)* 60, 397–404. doi:10.1016/0022-2364(84)90050-7
9. Hall AS, Barnard B, McArthur P, Gilderdale DJ, Young IR, and Bydder GM (1988) Investigation of a Whole-Body Receiver Coil Operating at Liquid Nitrogen Temperatures. *Magn Reson Med* 7, 230–5. doi:10.1002/mrm.1910070211
10. Hall AS, Alford NM, Button TW, Gilderdale DJ, Gehring KA, and Young IR (1991) Use of High Temperature Superconductor in a Receiver Coil for Magnetic Resonance Imaging. *Magn Reson Med* 20, 340–3. doi:10.1002/mrm.1910200218
11. Anderson WA, Brey WW, Brooke AL, Cole B, Delin KA, Fuks LF, et al. (1995) High-sensitivity NMR Spectroscopy Probe Using Superconductive Coils. *Bull Magn Reson* 17, 98–102.
12. Kovacs H, Moskau D, and Spraul M (2005) Cryogenically Cooled Probes-A Leap in NMR Technology. *Prog Nucl Magn Reson Spectrosc* 46, 131–55. doi:10.1016/j.pnmrs.2005.03.001
13. Niendorf T, Pohlmann A, Reimann HM, Waiczies H, Peper E, Huelnhagen T, et al. (2015) Advancing Cardiovascular, Neurovascular and Renal Magnetic Resonance Imaging in Small Rodents Using Cryogenic Radiofrequency Coil Technology. *Front Pharmacol* 6, 255. doi:10.3389/fphar.2015.00255
14. Wosik J, Xue L, Xie L-M, Kamel MR, Nesteruk K, and Bankson JA (2007) Superconducting Array for High-Field Magnetic Resonance Imaging. *Appl Phys Lett* 91, 183503. doi:10.1063/1.2801384
15. Nouls JC, Izenson MG, Greeley HP, and Johnson GA (2008) Design of a Superconducting Volume Coil for Magnetic Resonance Microscopy of the Mouse Brain. *J Magn Reson* 191, 231–8. doi:10.1016/j.jmr.2007.12.018
16. Lin I-T, Yang H-C, and Chen J-H (2012) Enlargement of the Field of View and Maintenance of a High Signal-To-Noise Ratio Using a Two-Element High-T C Superconducting Array in a 3T MRI. *PLoS One* 7, e42509. doi:10.1371/journal.pone.0042509
17. Ramaswamy V, Hooker JW, Withers RS, Nast RE, Brey WW, and Edison AS (2013) Development of a 13C-Optimized 1.5-mm High Temperature Superconducting NMR Probe. *J Magn Reson* 235, 58–65. doi:10.1016/j.jmr.2013.07.012
18. Laistler E, Poirier-Quinot M, Lambert SA, Dubuisson R-M, Girard OM, Moser E, et al. (2015) *In Vivo* MR Imaging of the Human Skin at Subnanoliter Resolution Using a Superconducting Surface Coil at 1.5 Tesla. *J Magn Reson Imaging* 41, 496–504. doi:10.1002/jmri.24549
19. Darrasse L, and Ginefri JC (2003) Perspectives with Cryogenic RF Probes in Biomedical MRI. *Biochimie* 85, 915–37. doi:10.1016/j.biochi.2003.09.016
20. Matula RA (1979) Electrical Resistivity of Copper, Gold, Palladium, and Silver. *J Phys Chem Reference Data*, 8(4), 1147–298. doi:10.1063/1.555614
21. Sondheimer EH (1952) The Mean Free Path of Electrons in Metals. *Adv Phys* 1, 1–42. doi:10.1080/00018735200101151
22. Wang Y, Su HT, Huang F, and Lancaster MJ (2007) Measurement of YBCO Thin Film Surface Resistance Using Coplanar Line Resonator Techniques from 20 MHz to 20 GHz. *IEEE Trans Appl Supercond* 17, 3632–9.
23. Anders S, Blamire MG, Buchholz F-I, Crété D-G, Cristiano R, Febvre P, et al. (2010) European Roadmap on Superconductive Electronics - Status and Perspectives. *Physica C: Superconductivity* 470, 2079–126. doi:10.1016/j.physc.2010.07.005
24. McFarland EW, and Mortara A (1992) Three-dimensional NMR Microscopy: Improving SNR with Temperature and Microcoils. *Magn Reson Imaging* 10, 279–88. doi:10.1016/0730-725X(92)90487-K
25. Black R, Early T, Roemer P, Mueller O, Mogro-Campero A, Turner L, et al. (1993) A High-Temperature Superconducting Receiver for Nuclear Magnetic Resonance Microscopy. *Science.* 259, 793–5. doi:10.1126/science.8430331
26. Miller JR, Zhang K, Ma QY, Mun IK, Jung KJ, Katz J, et al. (1996) Superconducting Receiver Coils for Sodium Magnetic Resonance Imaging. *IEEE Trans Biomed Eng* 43, 1197–9. doi:10.1109/10.544344
27. Ginefri J-C, Darrasse L, and Crozat P (2001) High-temperature Superconducting Surface Coil for *In Vivo* Microimaging of the Human Skin. *Magn Reson Med* 45, 376–82. doi:10.1002/1522-2594(200103)45:3<376::aid-mrm1049>3.0.co;2-r
28. Marek D. RF Receiver Coil Arrangement for NMR Spectrometers. US Patent 5247256A, 25 April 1990.
29. Hill HDW (1997) Improved Sensitivity of NMR Spectroscopy Probes by Use of High-Temperature Superconductive Detection Coils. *IEEE Trans Appl Supercond* 7, 3750–5. doi:10.1109/77.622233

30. Ratering D, Baltes C, Nordmeyer-Massner J, Marek D, and Rudin M (2008) Performance of a 200-MHz Cryogenic RF Probe Designed for MRI and MRS of the Murine Brain. *Magn Reson Med* 59, 1440–7. doi:10.1002/mrm.21629
31. Baltes C, Radzwill N, Bosshard S, Marek D, and Rudin M (2009) Micro MRI of the Mouse Brain Using a Novel 400 MHz Cryogenic Quadrature RF Probe. *NMR Biomed.* 22, 834–42. doi:10.1002/nbm.1396
32. Junge S (2012) Cryogenic and Superconducting Coils for MRI. *eMagRes* 1, 505–14.
33. Ginefri J-C, Poirier-Quinot M, Girard O, and Darrasse L (2007) Technical Aspects: Development, Manufacture and Installation of a Cryo-Cooled HTS Coil System for High-Resolution Iin-Vvivo Imaging of the Mouse at 1.5T. *Methods* 43, 54–67. doi:10.1016/j.ymeth.2007.03.011
34. Hu B, Varma G, Randell C, Keevil SF, Schaeffter T, and Glover P (2012) A Novel Receive-Only Liquid Nitrogen ($\Hbox{LN}_{2}$)-Cooled RF Coil for High-Resolution *In Vivo* Imaging on a 3-Tesla Whole-Body Scanner. *IEEE Trans Instrum Meas* 61, 129–39. doi:10.1109/TIM.2011.2157575
35. Lin I-T, Yang H-C, and Chen J-H (2013) A Temperature-Stable Cryo-System for High-Temperature Superconducting MR Iin-Vvivo Imaging. *PLoS One* 8, e61958. doi:10.1371/journal.pone.0061958
36. Sánchez-Heredia JD, Baron R, Hansen ESS, Laustsen C, Zhurbenko V, and Ardenkjaer-Larsen JH (2020) Autonomous Cryogenic RF Receive Coil for 13 C Imaging of Rodents at 3 T. *Magn Reson Med* 84, 497–508. doi:10.1002/mrm.28113
37. Vester M, Steinmeyer F, Roas B, Thummes G, and Klundt K (1997) High Temperature Superconducting Surface Coils with Liquid Nitrogen or Pulse Tube Refrigeration (Abstr). in Vancouver, BC: ISMRM 5th Scientific Meeting and Exhibition, doi:10.4095/219009
38. Darrasse L, Chiron L, Ginefri J-C, Poirier-Quinot M, Trollier T, Ravex A, et al. (2004) Cryosonde IRM : antenne IRM supraconductrice pour la microscopie des régions superficielles du corps humain et des petits modèles animaux. *ITBM-RBM* 25, 254–9. doi:10.1016/j.rbmret.2004.09.003
39. Lambert S, Ginefri J-C, Poirier-Quinot M, and Darrasse L (2013) High-temperature Superconducting Radiofrequency Probe for Magnetic Resonance Imaging Applications Operated below Ambient Pressure in a Simple Liquid-Nitrogen Cryostat. *Rev Scientific Instr* 84, 054701. doi:10.1063/1.4802947
40. Authelet G, Poirier-Quinot M, Ginefri J-C, Bonelli A, and Baudouy B (2017) Conceptual Design of a Cryogen-free μMRI Device. in *IOP Conf Ser Mater Sci Eng*, 12122.
41. Authelet G, Bonelli A, Poirier-Quinot M, Ginefri JC, Saniour I, and Baudouy B (2019) All Polymer Cryogen Free Cryostat for μ-MRI Application at Clinical Field. in *IOP Conf Ser Mater Sci Eng*, 12156.
42. Saniour I, Authelet G, Baudouy B, Dubuisson R-M, Jourdain L, Willoquet G, et al. (2020) A Temperature-Controlled Cryogen Free Cryostat Integrated with Transceiver-Mode Superconducting Coil for High-Resolution Magnetic Resonance Imaging. *Rev Scientific Instr* 91, 055106, doi:10.1063/1.5143107
43. Tinkham M (1996) *Introduction to Superconductivity*. 2nd ed. eds. J Shira and E Castellano New-York: McGraw-Hill.
44. Serfaty S, Haziza N, Darrasse L, and Kan S (1997) Multi-turn Split-Conductor Transmission-Line Resonators. *Magn Reson Med* 38, 687–9. doi:10.1002/mrm.1910380424
45. Díez-Sierra J, López-Domínguez P, Rijckaert H, Rikel M, Hänisch J, Khan MZ, et al. (2020) High Critical Current Density and Enhanced Pinning in Superconducting Films of YBa2Cu3O7−δ Nanocomposites with Embedded BaZrO3, BaHfO3, BaTiO3, and SrZrO3 Nanocrystals. *ACS Appl Nano Mater* 3, 5542–53. doi:10.1021/acsanm.0c00814
46. Shen ZY (1994) High-temperature Superconducting Microwave Circuits. Boston, MA: Artech House Publishers.
47. Girard O, Ginefri J-C, Poirier-Quinot M, and Darrasse L (2007) Method for Nonlinear Characterization of Radio Frequency Coils Made of High Temperature Superconducting Material in View of Magnetic Resonance Imaging Applications. *Rev Scientific Instr* 78, 124703. doi:10.1063/1.2825241
48. Geahel M (2018) *Découplage de détecteurs radiofréquences supraconducteurs à très haute sensibilité pour la micro-imagerie par résonance magnétique*. https://tel.archives-ouvertes.fr/tel-01880203/document (Accessed March 20, 2021).
49. Saniour I, Authelet G, Baudouy B, Dubuisson RM, van der Beek CJ, Darrasse L, et al. (2019) *Novel Passive Decoupling Approach for High Resolution HTS RF Coils Based on the Nonlinear Electrical Properties of Superconductors*. Rotterdam: ESMRMB 2019. in *36th Annual Scientific Meeting. Springer*.
50. Saniour I, Geahel M, Briatico J, Beek CJvan der, Willoquet G, Jourdain L, et al. (2020) Versatile Cryogen-free Cryostat for the Electromagnetic Characterization of Superconducting Radiofrequency Coils. *EPJ Tech Instrum* 7, 1–11. doi:10.1140/epjti/s40485-020-00055-2
51. Clem JR, and Sanchez A (1994) Hysteretic AC Losses and Susceptibility of Thin Superconducting Disks. *Phys Rev B* 50, 9355, 62. doi:10.1103/physrevb.50.9355
52. Frass-Kriegl R, Laistler E, Hosseinnezhadian S, Schmid AI, Moser E, Poirier-Quinot M, et al. (2016) Multi-turn Multi-gap Transmission Line Resonators - Concept, Design and First Implementation at 4.7 T and 7 T. *J Magn Reson*, 273, 65–72. doi:10.1016/j.jmr.2016.10.008
53. Ginefri J-C, Durand E, and Darrasse L (1999) Quick Measurement of Nuclear Magnetic Resonance Coil Sensitivity with a Single-Loop Probe. *Rev Scientific Instr* 70, 4730–1. doi:10.1063/1.1150142
54. Poirier-Quinot M, Frasca G, Wilhelm C, Luciani N, Ginefri J-C, Darrasse L, et al. (2010) High-resolution 1.5-Tesla Magnetic Resonance Imaging for Tissue-Engineered Constructs: a Noninvasive Tool to Assess Three-Dimensional Scaffold Architecture and Cell Seeding. *Tissue Eng C: Methods* 16, 185–200. doi:10.1089/ten.tec.2009.0015
55. Wright AC, Song HK, Elliott DM, and Wehrli FW (2005) Use of a Joule-Thomson Micro-refrigerator to Cool a Radio-Frequency Coil for Magnetic Resonance Microscopy. *Rev Scientific Instr* 76, 014301. doi:10.1063/1.1824340
56. Koo C, Godley RF, Park J, McDougall MP, Wright SM, and Han A (2011) A Magnetic Resonance (MR) Microscopy System Using a Microfluidically Cryo-Cooled Planar Coil. *Lab Chip* 11, 2197–203. doi:10.1039/c1lc20056a
57. Li Z, Willoquet G, Guillot Gv., Hosseinnezhadian S, Jourdain L, Poirier-quinot M, et al. (2016) Study of Two Contact-Less Tuning Principles for Small Monolithic Radiofrequency MRI Coils and Development of an Automated System Based on Piezoelectric Motor. *Sensors Actuators A: Phys.* 241, 176–89. doi:10.1016/j.sna.2016.02.008

Conflict of Interest: The authors declare that the research was conducted in the absence of any commercial or financial relationships that could be construed as a potential conflict of interest.